CHEMISTRY OF MATERIALS

Article

pubs.acs.org/cm

$CuSbS_2$ as a Promising Earth-Abundant Photovoltaic Absorber Material: A Combined Theoretical and Experimental Study

Bo Yang,[†] Liang Wang,[†] Jun Han,[†] Ying Zhou,[†] Huaibing Song,[†] Shiyou Chen,*[,‡] Jie Zhong,[†] Lu Lv,[§] Dongmei Niu,[§] and Jiang Tang*[,†]

[†]Wuhan National Laboratory for Optoelectronics (WNLO) and School of Optical and Electronic Information, Huazhong University of Science and Technology (HUST), Wuhan 430074, China

[‡]Key Laboratory for Polar Materials and Devices (MOE), East China Normal University, Shanghai 200241, China, and Physics Department, Fudan University, Shanghai 200433, China

[§]Institute of Super-microstructure and Ultrafast Process in Advanced Materials, School of Physics and Electronics, The Central South University, Changsha, Hunan 410083, China

Supporting Information

ABSTRACT: Recently, $CuSbS_2$ has been proposed as an alternative earth-abundant absorber material for thin film solar cells. However, no systematic study on the chemical, optical, and electrical properties of $CuSbS_2$ has been reported. Using density functional theory (DFT) calculations, we showed that $CuSbS_2$ has superior defect physics with extremely low concentration of recombination-center defects within the forbidden gap, espeically under the S rich condition. It has intrinsically p-type conductivity, which is determined by the dominant Cu vacancy (V_{Cu}) defects with the a shallow ionization level and the lowest formation energy. Using a hydrazine based solution process, phase-pure, highly crystalline $CuSbS_2$ film with large grain size was successfully obtained. Optical absorption investigation revealed that our $CuSbS_2$ has a direct band gap of 1.4 eV. Ultraviolet photoelectron spectroscopy (UPS) study showed that the conduction band and valence band are located at 3.85 eV and −5.25 eV relative to the vacuum level, respectively. As the calculations predicted, a p-type conductivity is observed in the Hall effect measurements with a hole concentration of ~10^{18} cm^{-3} and hole mobility of 49 $cm^2/(V\,s)$. Finally, we have built a prototype FTO/$CuSbS_2$/CdS/ZnO/ZnO:Al/Au solar cell and achieved 0.50% solar conversion efficiency. Our theoretical and experimental investigation confirmed that $CuSbS_2$ is indeed a very promising absorber material for solar cell application.

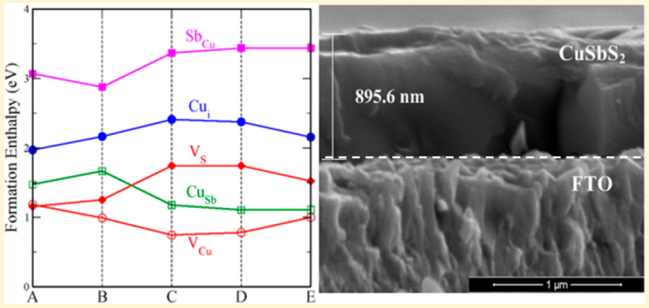

INTRODUCTION

Thin film photovoltaics have experienced significant research progress in last one year, with copper indium gallium selenide (CIGS) solar cell achieving 20.8%,[1] cadmium telluride (CdTe) solar cell achieving 19.6%,[1] and the new emerging organometal trihalide perovskite solar cell achieving 15.4%.[2] However, these photovoltaics suffer from either toxic elements (Cd in CdTe and Pb in perovskite) or scarcity of raw materials (In in CIGS and Te in CdTe), limiting their environmentally amenable, terawatt scale application. In consequence, low-toxicity and earth-abundant absorber materials for thin film photovoltaics are intensively explored including Cu_2O,[3] Cu_2S,[4] Fe_2S,[5,6] SnS,[7] $ZnSnP_2$,[8] Cu_2ZnSnS_4,[9] and $CuTaN_2$.[10] Among them, copper zinc tin sulfoselenide (CZTSSe) is most promising in terms of device efficiency, having achieved a certified 12.6% efficiency via a hydrazine-based solution process.[11]

Chalcostibite ($CuSbS_2$), a relatively less explored ternary I−V−VI_2 chalcogenide, is also proposed as a promising absorber material for sustainable and scalable photovoltaics for some reasons: (i) Both theoretical simulation and experimental investigation indicate that $CuSbS_2$ has a direct band gap of 1.38−1.5 eV falling within the optimum range for a single junction terrestrial solar cell.[12−15] It also has a high optical absorption coefficient of over 10^4 cm^{-1} and a spectroscopic limited maximum efficiency (SLME) of 22.9%, which was embodied in the pioneer work done by Liping Yu et al.[16] (ii) All elemental components of $CuSbS_2$ are low-toxic, earth-abundant, and economical. Supporting Information Figure S1 shows the relative abundance and prices of relevant raw materials, which indicates the distinct superiorities in abundance and price of Cu, Sb, and S raw materials compared to In, Ga, Te, and Cd. (iii) $CuSbS_2$ possesses a stable phase with a low melting point of 551 °C,[17] indicating the feasibility of grain growth at low temperature. This is also the reason why

Received: February 12, 2014
Revised: May 1, 2014
Published: May 5, 2014

   dx.doi.org/10.1021/cm500516v | Chem. Mater. 2014, 26, 3135−3143

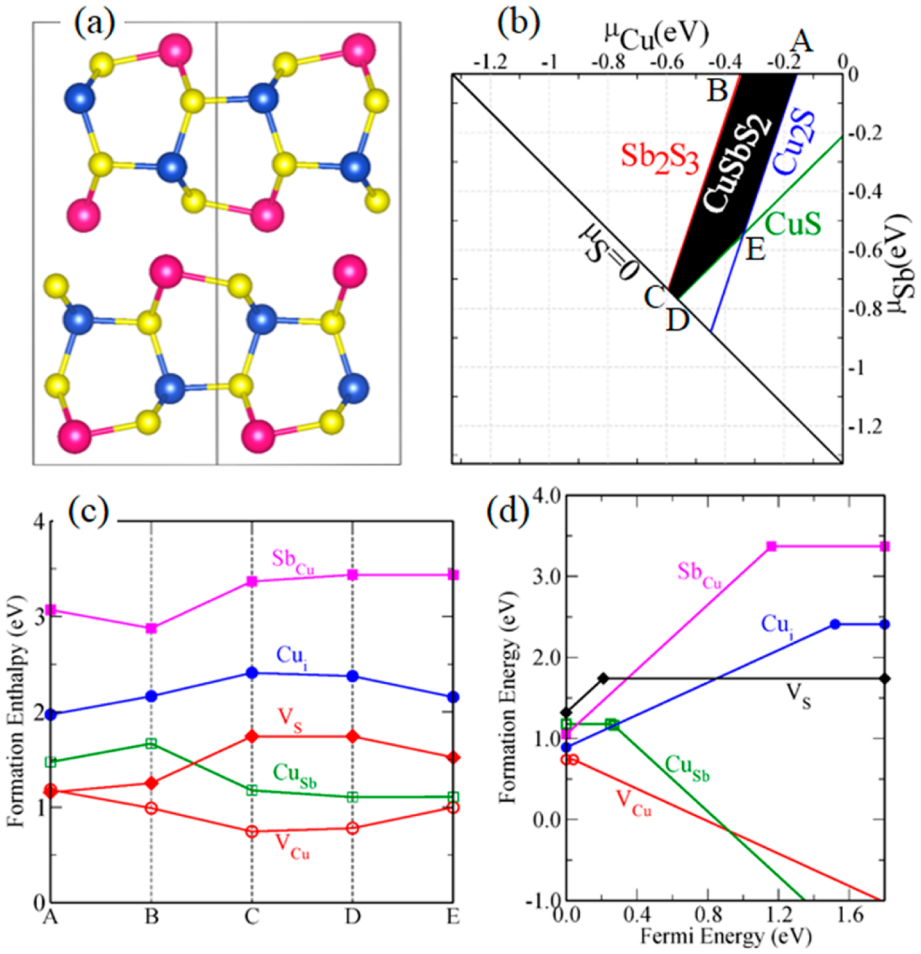

Figure 1. (a) Crystal structure of $CuSbS_2$, with two repeated primitive cells shown (blue, Cu; yellow, S; wine, Sb). (b) The calculated stable chemical-potential region of $CuSbS_2$ (the area surrounded by A, B, C, D, and E points). (c) The formation energy of neutral intrinsic defects in $CuSbS_2$ as a function of the chemical potential at points A, B, C, D, and E shown in panel b. (d) The formation energy of neutral and charged defects as a function of the Femi energy at the chemical-potential point C.

Sb was introduced into CIGS film to promote grain growth.[18] All of these characteristics merit exploration of $CuSbS_2$ for photovoltaic application.

Attracted by its promising application, a series of different techniques, such as spray pyrolysis,[19] thermal evaporation,[20,21] chemical bath deposition followed by annealing treatment,[15,22] and electrodeposition,[21,23] have been recently reported to deposit $CuSbS_2$ films. However, most of these reports provided limited photovoltaic-relevant film characterization and some focused on thermoelectric application,[24,25] only two studies presented the application of this material for thin film solar cells.[26,27] Many key parameters of $CuSbS_2$, such as the conduction band and valence band position and the intrinsic defect physics, remain unclear at present. A detailed investigation to better understand the photovoltaic-relevant properties of $CuSbS_2$ film is thus urgently needed.

To meet this demand, in this article, we have systematically (both theoretically and experimentally) investigated the chemical, optical, and electrical properties of $CuSbS_2$ and fully evaluated its potential for solar cell application. Specifically, we first applied density functional theory (DFT) calculations to study the defect physics of $CuSbS_2$. Guided by the theoretical results, we then fabricated high quality $CuSbS_2$ film using a hydrazine process and carefully studied its chemical, optical, and electrical properties, and finally, we built a prototype solar cell employing the CIGS device configuration. Our combined investigation confirmed that $CuSbS_2$ is indeed a very promising absorber material for thin film solar cells.

EXPERIMENTAL SECTION

Chemicals. Copper powder (Cu, 99.999%), antimony powder (Sb, 99.999%), and sulfur pieces (S, 99.999%) were all purchased from Alfa Aesar. Anhydrous hydrazine (N_2H_4, 98%) was purchased from Sinopharm Group Co. Ltd. All chemicals were used as received.

Preparation of $CuSbS_2$ Precursor Solution. All experiments were done in a nitrogen filled glovebox (oxygen and water concentration maintained below 1 ppm). ***Caution!*** *Hydrazine is highly toxic and should be handled in the glovebox with great caution.*[28,29] To prepare the Cu−S stock solution, 0.226 g of Cu, and 0.175 g of S were dissolved in 2 mL hydrazine, which would produce a clear orange solution after magnetic stirring for a few days. Analogously, 0.484 g of Sb and 0.445 g S were dissolved in 2 mL hydrazine, which produced a clear yellow Sb−S solution after stirring for a few days. The final Cu−Sb−S solution was prepared by mixing the Cu−S and Sb−S stock solution together with the desired Cu/Sb molar ratio of 0.9:1, yielding a clear deep orange solution with some viscosity. Before thin film deposition, the final Cu−Sb−S solution should be stirred for at least 2 h.

Film Deposition and Device Fabrication. $CuSbS_2$ films were deposited on 3 × 3 cm^2 FTO substrates by spin coating (500 rpm for 10 s, 2100 rpm for 45 s). After spin-coating, the film was dried on a

dx.doi.org/10.1021/cm500516v | *Chem. Mater.* 2014, 26, 3135−3143

preheated hot plate at 100 °C for 10 min and subsequently annealed at 250 °C for 3 min (soft bake). The spin-coating and soft-bake process was repeated for another 4 times to produce a film of ~1 μm thickness (approximately 200 nm per layer). Finally, the film was annealed at 350 °C for 10 min (final bake) and carefully cooled. For photovoltaic device fabrication, as-prepared $CuSbS_2$ film was subjected to a chemical bath deposition of 50 nm thick CdS layer using a literature method.[30] Subsequently, the window layers of intrinsic ZnO (50 nm) and ZnO:Al (400 nm) were deposited by radio frequency sputtering. At last, gold contacts (approximately 50 nm thick) were deposited by thermal evaporation (Beijing Technol Science Co. Ltd.) at a rate of 0.05 Å/s. Total device area was 0.45 cm^2 defined by mechanical scribing, and the active device area was 0.40 cm^2 (subtracting the electrode shadow area).

Materials and Device Characterization. $CuSbS_2$ thin films prepared on FTO glass were characterized by XRD (Philips, X pert pro MRD, with Cu Kα radiation, λ = 1.54178 Å), AES (Physical Electronics Model 670 field emission scanning Auger microprobe, a 5 kV, 20 nA primary electron beam was used in conjunction with a 3 kV Ar^+ ion beam). XPS (EDAX Inc. Genesis), UPS (Specs UVLS, He I excitation, 21.2 eV, referenced to the Fermi edge of argon etched gold), SEM (FEI Nova NanoSEM450, without Pt coating), Hall effect (Ecopia HMS-5500, with gold electrodes) and absorption (PerkinElmer Instruments, Lambda 950 using integrating sphere). The Cu−Sb−S precursor powder, which was obtained from naturally drying the Cu−Sb−S precursor solution, was characterized by TGA and DSC (PerkinElmer Instruments, Diamond TG/DSC6300, ramp rate 2 °C/min, N_2 flowing environment). Device performance was measured under a solar simulator with a Xe light source (450 W, Oriel, model 9119) and an Air Mass 1.5G filter, which could provide simulated 1 sun illumination. No intentional temperature control or aparture was used for the efficiency measurement.

Calculation Methods. The phase stability and defect properties are studied using the first-principles calculation based on the density functional theory (DFT) formalism, with the structural relaxation and electronic structure calculations performed using the VASP code. The frozen-core projector augmented-wave (PAW) pseudopotentials were employed with an energy cutoff of 350 eV for the plane wave basis set. A 4 × 8 × 2 Monkhorst−Pack k-point mesh is included in the Brillouin zone integration for the 16-atom primitive cell and a 2 × 2 × 2 mesh is included for the 96-atom supercell, which is used for the simulation of defects. Test calculations with denser k-point mesh show the results are well converged. For the exchange-correlation functional, we used the nonlocal hybrid functional (HSE06) for the structural relaxation and band structure calculation of the primitive cell as well as the study of defects with large supercell. We also compared the defect formation energies and transition energy levels calculated using the semilocal GGA and hybrid functionals, which showed that the main conclusions about the dominant defects and their transition energy levels are independent of the specific functionals that we used.

RESULTS AND DISCUSSION

Theoretical Simulation: Phase Stability and Defect Physics. We first discuss the phase stability and defect physics of $CuSbS_2$ from our first-principles simulation. In Figure 1a, we plot the crystal structure of $CuSbS_2$, where the Cu and Sb cations are ordered and intermixed in the ideal lattice of the ternary compound. However, in the synthesis, the starting precursors are usually the mixture of elemental (Cu, Sb, S) or binary phases (Sb_2S_3, CuS, and Cu_2S), and whether they can react and form the ternary $CuSbS_2$ compound depends on the competition of their formation energies. This competition can be quantitatively described by the limit to the chemical potentials of the component elements,[31] that is, μ_{Cu}, μ_{Sb}, and μ_S for $CuSbS_2$. If $CuSbS_2$ is stabilized and can be synthesized without the coexistence of the element or binary secondary phases, μ_{Cu} and μ_{Sb} are limited in a range as shown by the black region in Figure 1b [μ_S are dependent on them under equilibrium]. When the chemical potential is in the black region, single-phase $CuSbS_2$ is stabilized in the synthesis environment, but when it goes beyond this range, other compounds such as Sb_2S_3, Cu_2S, and CuS will be generated. Comparing the stable region of $CuSbS_2$ to that of Cu_2ZnSnS_4, it is as narrow as that of Cu_2ZnSnS_4,[31] indicating that the composition control should also be important for the synthesis of single-phase $CuSbS_2$ samples. Because of the competition of Cu_2S and Sb_2S_3, the stable region is especially narrow along the μ_{Cu} axis (the width is less than 0.2 eV), and thus, the control of Cu composition should be critical. The coexistence of Sb_2S_3, CuS, Cu_2S, Cu, and Sb metals are highly possible if the samples are nonstoichiometric.

When the chemical potential is in the stable region, the synthesized samples should be single-phase crystals of $CuSbS_2$; however, the existence of intrinsic point defects is still possible, which is determined by their formation energies. The formation energies depend on the chemical potentials of the related elements (richness of the elements in the environment); that is, when a element is rich, it is difficult to form a vacancy of the element by removing an atom from the lattice to the environment, and vice versa. Our calculated formation energies of possible point defects are listed in Figure 1c, which change with the chemical potentials, along the A−B−C−D−E path in Figure 1b (the detailed numbers are given in the Supporting Information, Table 1S). Obviously, the acceptor defect V_{Cu} (Cu vacancy) has the lowest formation energy under most of the chemical potential conditions, and only when the chemical potential is near the A point (a Cu-rich, Sb-rich, and S-poor condition), the formation energy of the donor defect V_S (S vacancy) becomes close to that of V_{Cu}. Our following calculations showed that V_{Cu} is a shallow acceptor that can be ionized easily and generate free hole carriers under room temperature, while V_S is a deep donor with its ionization level far from the conduction band (near the valence band) and cannot generate free electron carriers, so the conductivity should be determined mainly by the V_{Cu} acceptors, and the synthesized samples should be intrinsically p-type no matter under S-rich or S-poor condictions. Other acceptor defects such as Cu_{Sb} (Cu on Sb antisite) and donor defects such as Sb_{Cu} and Cu_i (Cu interstitial) always have higher formation energy than V_{Cu}, so their influence on the conductivity is smaller.

In Figure 1d, we also plot the formation energies of these defects when they are ionized at different charge states (at the chemical potential point C, which corresponds to the S-rich condition that is used in our preparation of $CuSbS_2$ films). The formation energies of the ionized defects depend on the Fermi energy of the samples, that is, those of charged acceptors (donors) decrease (increase) when the Fermi energy shifts up from the valence band maximum (VBM) to the conduction band minimum (CBM). Because the formation energy of the ionized V_{Cu} acceptor decreases to zero when the Fermi energy is at about 0.8 eV above VBM, it will form spontaneously to compensate any n-type donor defects or dopants and pin the Fermi energy to below the middle of the gap (it is difficult to shift the Fermi energy to higher than this pinning level through introducing donor defects or dopants). Based on this, we predict that it is difficult to dope $CuSbS_2$ to n-type under the S-rich condition (it is also difficult under the S-poor condition, but the pinning level of Fermi energy is higher, at about 1.1 eV above VBM).

The turning points in Figure 1d for different defects show their transition energy levels. The (−/0) level of the dominant

dx.doi.org/10.1021/cm500516v | Chem. Mater. 2014, 26, 3135−3143

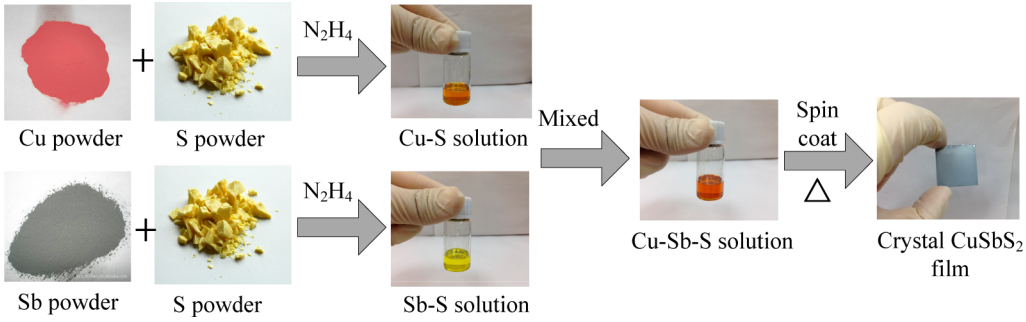

Figure 2. Flow diagram of synthetic route to $CuSbS_2$ thin films.

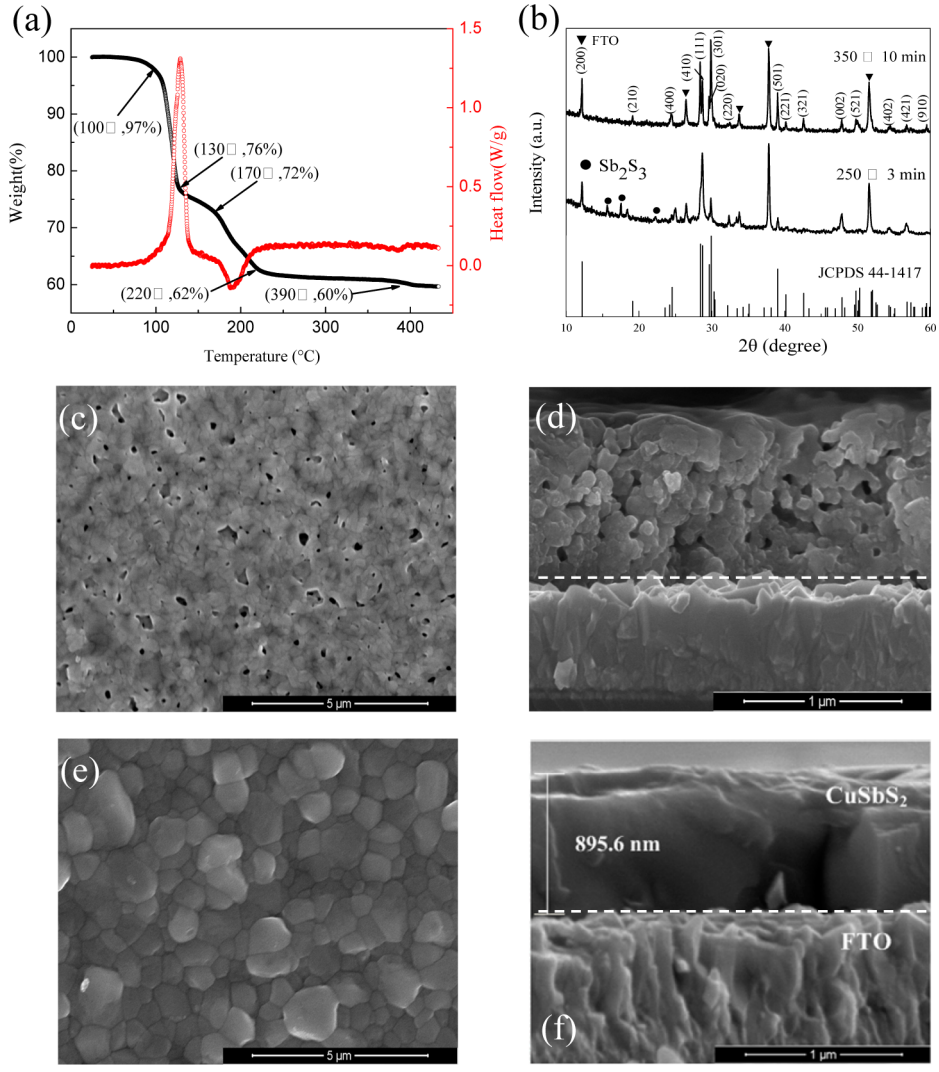

Figure 3. (a) TGA and DSC scans of the $CuSbS_2$ precursor powder (ramp rate 2 °C/min, N_2 flowing environment). Exothermal peaks are down along the heat flow axis. (b) XRD patterns of the $CuSbS_2$ thin films on FTO substrate after soft-bake (250 °C for 3 min) and final-bake (350 °C for 10 min). The peaks marked with ▼ and ● are FTO and Sb_2S_3, respectively. The bottom showed the standard diffraction pattern of $CuSbS_2$ (JCPDS 44-1417). The top-view and cross-sectional SEM images of $CuSbS_2$ films after soft-bake (c and d) and after final-bake (e and f). White dash lines delineates FTO substrate and $CuSbS_2$ film.

acceptor defect V_{Cu} is very shallow, 0.03 eV above VBM, which means that V_{Cu} defects can be easily ionized under room temperature. This is similar to the situation in other Cu-based sulfide or selenide semiconductors such as $Cu_2ZnSnSnS_4$ and $CuInSe_2$ where V_{Cu} also has a shallow level around 0.02 eV.[31] The ionization of one V_{Cu} defect gives birth to one hole carrier. When the chemical potential is at the chemical potential point C (S-rich condition), the neutral V_{Cu} has a formation energy around 0.8 eV, and the ionized V_{Cu} has a formation energy around 0.6 eV if the Fermi energy is at 0.2 eV above VBM. Based on this, we estimate that the hole concentration generated by V_{Cu} should be on the order of 10^{17}–10^{18} cm^{-3} under a growth temperature around 300 °C. Another acceptor defect Cu_{Sb} has deeper level than V_{Cu}, but it is not so deep

dx.doi.org/10.1021/cm500516v | Chem. Mater. 2014, 26, 3135−3143

(0.25 eV). On the donor defect side, Cu_i has the shallowest donor level and also has the lowest formation energy when ionized, about 1.1 eV when Fermi energy is 0.2 eV above VBM. V_S and Sb_{Cu} have deep donor levels, and their formation energies are higher than 1.5 eV when Fermi energy is 0.2 eV above VBM. The very deep donor level of V_S (close to VBM, far from the middle of the gap or CBM) makes it difficult to generate free electron carriers, so the existence of V_S does not give rise to n-type intrinsic conductivity. Considering that all low-energy defects have levels far from the middle of the band gap (espeically under S-rich condition), $CuSbS_2$ can be considered as a good solar cell absorber semiconductor free of recombination-center defects, in contrast with other absorber semiconductors such as $CuGaSe_2$ and Cu_2ZnSnS_4, which have recombination-center defects.[31,32]

Hydrazine Processed $CuSbS_2$ Film Fabrication. Given the suitable band gap and benign defect properties, we now turn to the experimental investigation of $CuSbS_2$ film. Similar to our previous report on Sb_2Se_3 solar cells,[33] we applied hydrazine-based solution process to fabricate $CuSbS_2$ films. Hydrazine is a solvent capable of dissolving metal chalcogenides (e.g., SnS_2, Cu_2S, In_2Se_3) at room temperature without the introduction of unintentional impurities. Via a moderate heat-treatment, these hydrazinium-based precursors decompose into the desired metal chalcogenide films with tight stoichiometry and phase control.[34−37] High-mobility ultrathin SnS_xSe_{2-x}[38] and In_2Te_3[39] films for transistors and high-efficiency CIGS and CZTSSe solar cells[40,41] were achieved through this hydrazine-based process.

In our process, metals and sulfur (Cu, Sb, and S) instead of traditional metal sulfide[42,43] were chosen as the precursors because commercial cuprous sulfide often contain non-stoichiometric components such as $Cu_{2-x}S$, which seriously hamper consistent and precise composition control. Guided by the theoretical simulation result that V_{Cu} is the main source of acceptors in $CuSbS_2$ film, we employed a Cu/Sb molar ratio of 0.9 for film preparation in order to produce p-type films. Deposition of $CuSbS_2$ films involved four steps (as shown in Figure 2): (i) dissolve the individual metal powder (e.g., Cu, Sb) with sulfur in anhydrous hydrazine to produce the Cu−S and Sb−S stock solutions at room temperature; (ii) prepare the final Cu−Sb−S precursor solution by mixing the Cu−S and Sb−S solutions, followed by stirring for at least 2 h before spin-coating; (iii) spin-coat Cu−Sb−S precursor solution onto precleaned FTO substrates to produce thin films; (iv) anneal as-deposited thin films with proper temperature and duration to remove excess S and yield the $CuSbS_2$ final products. In our process, Cu−S, Sb−S, and Cu−Sb−S all completely dissolved into hydrazine and formed clear solutions, indicating mixing of these atoms on a molecular level. Such a molecular-scale homogeneity of precursor solution facilitated fabrication of $CuSbS_2$ film with excellent uniformity over large dimensions, which was proven to be very important for $CuSbS_2$ solar cells.[27]

We turned to thermogravimetric analysis (TGA) and differential scanning calorimetry (DSC) to find the appropriate baking conditions. Figure 3a shows TGA and DSC data for the Cu−Sb−S precursor powder. As seen in Figure 3a, the Cu−Sb−S precursor decomposes endothermically with an onset at ∼100 °C, followed by a second broad exothermic process at higher temperature, ultimately leading to reaction of the precursor into the expected film. The weight loss and the endothermic peak at low temperature (100 °C < T < 130 °C) represented evaporation of free hydrazine and dissociation of hydrazinium species from the precursor solutions; weight loss at higher-temperature (130 °C < T < 220 °C) corresponded to the leaving of excess sulfur held within the films.[42,44,45] The corresponding exothermic peak at this temperature is probably originated from the reaction of Cu_2S with Sb_2S_3 into $CuSbS_2$. At T > 220 °C, both TGA and DSC curves turned into flat suggesting $CuSbS_2$ phase should be produced at this temperature. Based on TGA analysis, we designed a two-stage annealing process to produce $CuSbS_2$ film: one soft-bake at 250 °C for 3 min to eliminate excess hydrazine and sulfur and one final-bake at 350 °C for 10 min to promote grain growth. Annealing details are included in the Experimental Section, and the corresponding X-ray diffraction (XRD) patterns for the soft-baked and final-baked $CuSbS_2$ thin films are shown in Figure 3b. The pattern for soft-baked film confirmed that as-deposited film was $CuSbS_2$ (JCPDS 44-1417); however, there were three peaks assignable to Sb_2S_3 (JCPDS 42-1393). This observation echoes previous simulation results that $CuSbS_2$ coexists with Sb_2S_3 when μ_{Cu} is low, which is the case here because our precursor solution is Cu deficient. When as-deposited film was further annealed at 350 °C for 10 min, XRD pattern was in perfect agreement with orthorhombic $CuSbS_2$ (JCPDS 44-1417), indicating we obtained phase-pure $CuSbS_2$ without any impurities or secondary phase. This phenomenon is explainable by the high vapor pressure of Sb_2S_3: excess Sb_2S_3 left the film during final-bake, similar to the SnS/SnS_2 loss in CZTS film during high temperature annealing.[46] The refined orthorhombic lattice parameters for the final-baked $CuSbS_2$ film, derived from the full diffraction pattern except FTO peaks, were a = 6.024 Å, b = 3.786 Å, c = 14.701 Å, which were in good agreement with the published values.[47,48]

We applied scanning electron microscopy (SEM) to characterize the morphology of soft-baked and final-baked $CuSbS_2$ films, and the results are presented in Figure 3c, d and e, f, respectively. After soft-bake, both top-view and cross-sectional SEM images showed the formation of poor-quality film with voids abundantly presented. The grain size of $CuSbS_2$ was also quite small in the vicinity of one hundred nanometers. After 350 °C bake for 10 min, top-view SEM characterization revealed a crack- and pinhole-free film; cross-sectional SEM image showed a compact $CuSbS_2$ film with large grains close to one micrometer. Clearly, significant grain coalescence occurred during the final bake, squeezing out the voids and increasing grain size significantly. XRD and SEM characterization confirmed the formation of phase-pure, large-grain, crack- and pinhole-free $CuSbS_2$ film after a short annealing at 350 °C, a temperature that is significantly lower than those employed in typical metal chalcogenide (e.g., CZTS[45] and CIGS[49]) and in $CuSbS_2$ film derived by other methods (e.g., 450 °C 30 min H_2S sulfurization[27]). This is consistent with the low melting point of $CuSbS_2$ and the mixing of component atoms at molecular levels in our hydrazine precursor solution. Such a low grain-growth temperature promises the potential integration of $CuSbS_2$ for flexible solar cells through an energy efficient way.

To obtain high quality $CuSbS_2$ film, our investigation indicated that we have to avoid: (i) high annealing temperature above 450 °C. At this temperature or above, $CuSbS_2$ film is close to melting, facilating droplet formation due to active thermal movement, as evidenced by the observation of abundant islands in SI Figure S2. (ii) High sulfur surplus. When Sb−S stock solution with S:Sb moral ratio higher than 3.5, large amount of excess sulfur is removed during the soft-bake and final-bake, leading to the formation of voids due to

dx.doi.org/10.1021/cm500516v | Chem. Mater. 2014, 26, 3135−3143

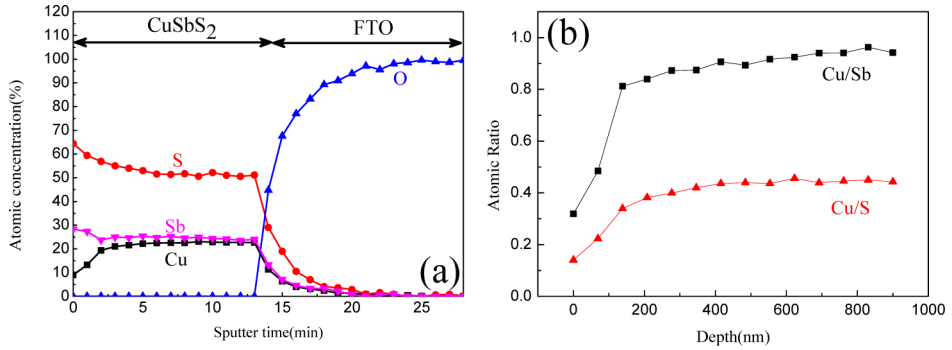

Figure 4. (a) AES depth profile of the resulting $CuSbS_2$ film on FTO substrate after final-bake (350 °C for 10 min). (b) The atomic ratio distribution of Cu/Sb and Cu/S along the depth of the $CuSbS_2$ film.

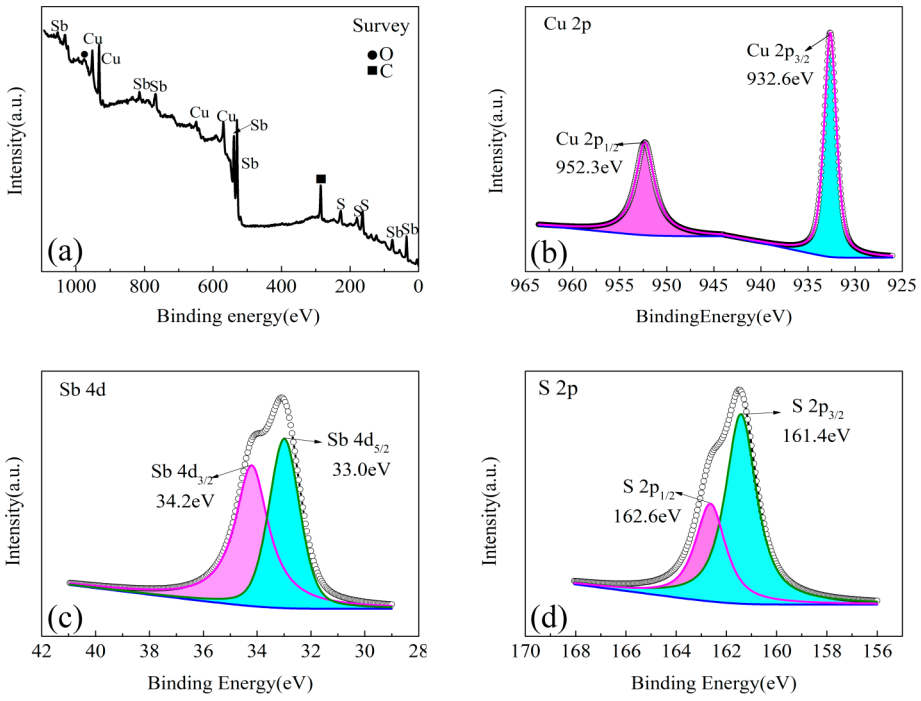

Figure 5. X-ray photoelectron spectra (XPS) of the $CuSbS_2$ films after final bake. (a) XPS survey spectrum of the $CuSbS_2$ films. (b~d) Magnified XPS spectra of copper, antimony, and sulfur (black lines). The fits were also shown (red, green, and blue lines). All the spectra were doublets in the expected positions of Cu, Sb, and S.

significant volume shrinkage (see SI Figure S3). This is the reason why we used Sb/S ratio of 1:3.5 and only annealed $CuSbS_2$ film at 350 °C to get the best quality $CuSbS_2$ film.

Auger electron spectrocopy (AES) measurement was used to analyze the elemental distribution along the depth of our $CuSbS_2$ film. Figure 4 shows the Cu, Sb, and S elemental depth profile and the derived Cu/Sb and Cu/S atomic ratio depth profile of $CuSbS_2$ film deposited on FTO substrate after final-bake. Without regard to the surface composition, AES results revealed that the bulk of our $CuSbS_2$ film showed homogeneous distribution of the studied elements after final-bake. Interestingly, a S rich and Sb rich region was detected close to the surface, which is probably caused by the trace amounts of Sb_2S_3 and S condensed from their vapor phases onto the film surface during the cooling process of final-bake.

Material, Optical, and Electrical Characterization of $CuSbS_2$ Film. Having proven that we have obtained phase-pure $CuSbS_2$ successfully, we applied X-ray photoelectron spectrum (XPS) to study the chemical nature of our film. The results are given in Figure 5. Elemental survey confirmed the presence of copper, antimony, and sulfur in the film. Careful inspection of the survey spectrum revealed the presence of trace amount of carbon and oxygen, which could be attributed to atmospheric O_2, CO_2, and H_2O absorption during sample preparation. Magnified XPS spectra of Cu, Sb, and S are shown in Figure 5b–d. Copper core-level spectrum showed a 2p doublet at the binding energy of 932.6 eV ($2p_{3/2}$) and 952.3 eV ($2p_{1/2}$) with a separation of 19.7 eV, which are in good agreement with Cu^+,[50,51] as expected for the $CuSbS_2$. Absence of Cu^{2+} was confirmed by the absence of Cu $2p_{3/2}$ peaks at 936 and 942 eV (satellite), Cu $2p_{1/2}$ peaks at 955 and 965 eV (satellite).[52] Antimony core-level spectrum showed a 4d doublet with an excellent fitting at the binding energy of 33.0 eV ($4d_{5/2}$) and 34.2 eV ($4d_{3/2}$) with a separation of 1.2 eV, which are in consistent with Sb^{3+}.[53] Absence of Sb^{5+} was confirmed by the absence of peaks at 35.5 eV (Sb $4d_{5/2}$) and 36.7 eV (Sb $4d_{3/2}$).[53] Similarly, sulfur core-level spectrum showed S $2p_{3/2}$ peak at 161.4 eV and $2p_{1/2}$ peak at 162.6 eV

dx.doi.org/10.1021/cm500516v | Chem. Mater. 2014, 26, 3135−3143

with a separation of 1.2 eV. The positions, separations and relative intensities of the doublet peaks (2:1) were in good agreement with S^{2-}.[51,52] In the Cu−Sb−S system, there are another three ternary phases: Cu_3SbS_3, $Cu_{12}Sb_4S_{13}$, and Cu_3SbS_4.[54] Formation of latter two compounds requires an intemediate compound,[17] Cu_3SbS_3, which only form in Cu rich environment. However, our precursor solution was Cu deficient, thus ruling out the possibility of Cu_3SbS_3, $Cu_{12}Sb_4S_{13}$, and Cu_3SbS_4 formation.[54] Hence, XPS analysis further confirmed we obtained phase-pure $CuSbS_2$, and the normal valence state for this compound is $Cu^{+}Sb^{3+}S_2^{2-}$.

In order to determine the absorption coefficient α, optical transition type (direct or indirect) and optical band gap of $CuSbS_2$, transmission spectrum of $CuSbS_2$ film on FTO substrate was measured in the wavelength ranging from 600 to 1200 nm, as shown in Figure 6a. Transmittance steeply dropped at the wavelength of approximately 900 nm and decreased to zero at the wavelength shorter than 800 nm. Based on this spectrum, we further calculated the absorption coefficient α dependent on wavelength using the following simplified formula:[55] $\alpha = d^{-1}\ \mathrm{In}(T^{-1})$ where d is the thickness of the $CuSbS_2$ film determined by the SEM measurement, T is the measured film transmittance data. As shown in Figure 6b, the absorption coefficient for $CuSbS_2$ reaches 7×10^4 (cm^{-1}) for approximately 1.6 eV photons (wavelength of 775 nm), which conformed to the previous prediction[16] and was comparable to chalcopyrite or kesterite materials.[56−58] Furthermore, absorption coefficient α of a semiconductor material is related to its band gap E_g according to the following equation $(\alpha h\nu)^n = A^n(h\nu - E_g)$ where A is a constant, h is the Planck's constant, ν is the frequency of the incident photon and n equals to 2 for direct band gap semiconductors and to $^1/_2$ for an indirect band gap semiconductor.[59] We thus plotted $(\alpha h\nu)^2$ versus $h\nu$ (Figure 6b, inset) and obtained a linear fitting line with its extrapolation to the x-intercept at 1.4 eV. It should be noted that in the $(\alpha h\nu)^{1/2}$ versus $h\nu$ plotting no linear fitting could be generated. We thus conclude our $CuSbS_2$ film has a direct band gap of 1.4 eV, which agrees reasonably well with literature values.[16,47,60]

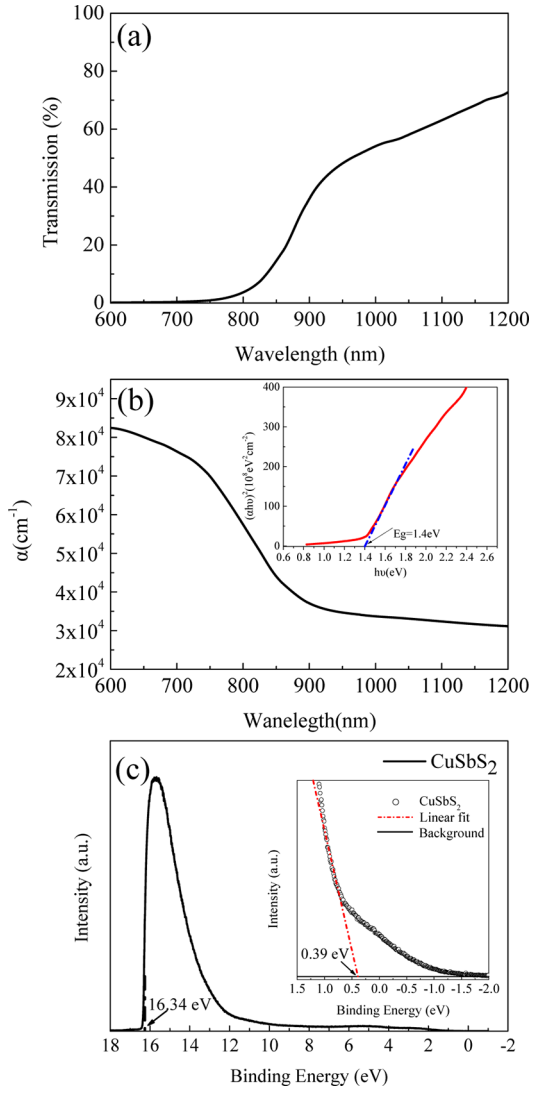

Figure 6. Optical and electrical properties of $CuSbS_2$ film annealed at 350 °C. (a) Transmission spectrum of $CuSbS_2$ film onto FTO conductive glass pieces. (b) Wavelength dependent absorption coefficient of $CuSbS_2$ film. Insert, Tauc plot (n = 2, direct) for $CuSbS_2$ film. (c) UPS spectra of $CuSbS_2$ film. The inserts showed the magnified spectra and linear fitting in the range −2.0−1.5 eV.

We also applied ultraviolet photoelectron spectroscopy (UPS) to determine the VBM and Fermi energy of our $CuSbS_2$ film. Au was deposited on $CuSbS_2$ film for calibration and the UPS result is given in Figure 6c. The Femi energy of $CuSbS_2$ was established as −4.86 eV, derived by subtracting the intercept at binding energy of 16.34 eV with the ultraviolet photon energy (He I excitation, 21.2 eV). Linear fitting of the UPS spectrum in the long tail generated an extrapolation of 0.39 eV, which corresponded to the distance between Fermi energy and VBM. Using the measured band gap of 1.4 eV from transmission spectra, we thus calculated the VBM at −5.25 eV, and the CBM at −3.85 eV, respectively. The position of the Fermi energy closer to the valence band confirmed the p-type nature of our $CuSbS_2$ film.

The Hall effect was further investigated to measure the electrical properties of $CuSbS_2$ film. Samples were prepared by depositing $CuSbS_2$ film onto quartz wafer with Au electrodes evaporated at four corners. The value of the Hall coefficient R_H was positive (2.35 cm^3/C) indicating p-type conduction for our $CuSbS_2$ film, in good agreement with the conclusion from UPS analysis and simulation prediction. By using the Van Der Pauw method,[61] the resistivity, hole mobility and doping density were estimated to be 4.8×10^{-2} Ω cm, 49 $cm^2/(V\ s)$ and 2.66×10^{18} cm^{-3}, respectively. Our hole mobility is larger than that reported previously,[16,62] which is probably due to the high quality of our $CuSbS_2$ film. Furthermore, the measured high hole concentration supported our calculated results that the dominant acceptor in $CuSbS_2$ is V_{cu} with low formation energy. A summary of the material properties of our $CuSbS_2$ film was enumerated in SI Table 1S.

Prototype $CuSbS_2$ Photovoltaic Device Performance. Finally, we tested our $CuSbS_2$ film in a full photovoltaic device. Device configuration is glass/FTO/$CuSbS_2$/CdS/ZnO/ZnO:Al/Au, as shown in Figure 7a. CdS layer was produced by the standard chemical bath deposition, ZnO and ZnO:Al were deposited using magentron sputtering, and Au electrodes were fabricated using thermal evaporation. From UPS analysis, our $CuSbS_2$ is p-type and has a VBM at −5.25 eV and a CBM at −3.85 eV. For CdS, VBM locates at −6.38 eV and CBM locates at −3.98 eV.[63] Therefore, $CuSbS_2$ and CdS could form a type-II staggered heterojunction facilitating charge separation, which is necessary for high efficiency solar cell. In addition, we

dx.doi.org/10.1021/cm500516v | Chem. Mater. 2014, 26, 3135−3143

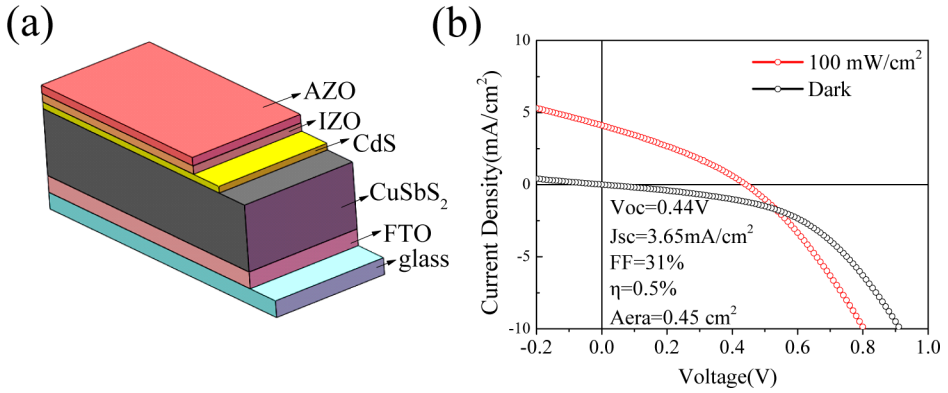

Figure 7. Photovoltaic device structure and electrical characteristics. (a) Schematic of device structure. (b) Current−density versus voltage curves of the CAS solar cell performance in the dark (black line) and under 100 mW/cm^2 simulated AM 1.5G irradiation (red line).

tested the $I-V$ characteristic of the contact between $CuSbS_2$ film and FTO substrate (SI Figure S4). The $I-V$ characteristic is linear under dark, demonstrating that good Ohmic contact has been obtained between $CuSbS_2$ film and FTO substrate. Light (100 mW/cm^2, simulated AM 1.5G irradiation) and dark current-density versus voltage ($J-V$) characteristics are presented in Figure 7b for our champion solar cell. This device exhibited a short-circuit current density (J_{sc}) of 3.65 mA/cm^2, an open-circuit voltage (V_{oc}) of 0.44 V, and a fill factor (FF) of 31%, which yielded a total area power conversion efficiency of 0.50%. The size of this device is 0.45 cm^2 defined by mechanical scribing. Our device efficiency was quite low, mainly limited by the poor $CuSbS_2$/CdS heterojunction as evidenced by the low rectification of $J-V$ curve in the dark, and also limited by the less-optimized ZnO and ZnO:Al sputtering process as evidenced by the low FF. Our device efficiency, however, is still encouraging considering very limited optimization work done so far. Improvement in $CuSbS_2$ film quality, interface engineering, ZnO and ZnO:Al sputtering was underway in order to further boost device efficiency.

CONCLUSIONS

In summary, we have provided a detailed theoretical and experimental investigation of $CuSbS_2$, a promising absorber material for earth-abundant thin film photovoltaics. DFT simulation indicated that $CuSbS_2$ was intrinsically p-type with shallow V_{Cu} defects being the dominant acceptors. The formation energy and defect depth of acceptors (V_{Cu} and Cu_{Sb}) and donors (Cu_i, Sb_{Cu}, and V_S) in $CuSbS_2$ were also well documented. Phase-pure $CuSbS_2$ film with micrometer size grains was produced through the hydrazine solution process with a mild 350 °C thermal annealing. As-deposited film was determined to be direct band gap (E_g = 1.4 eV), has a hole concentration of ~10^{18} cm^{-3} and hole mobility of 49 cm^2/(V s), and the CBM and VBM locates at −3.85 eV and −5.25 eV, respectively. Finally, a prototype FTO/$CuSbS_2$/CdS/ZnO/ZnO:Al/Au solar cell was produced, achieving 0.50% solar conversion efficiency. Earth-abundant and low-toxic constituents, attractive optical and electrical properties, and benign defect physics enable $CuSbS_2$ a very attractive absorber candidate for thin film photovoltaics, and our detailed study deepened the understanding of $CuSbS_2$ film and paved the way for their future promising application.

ASSOCIATED CONTENT

Supporting Information

Comparison of elemental abundance and prices, and SEM images of $CuSbS_2$ films finally annealed at different temperature and using different Sb/S ratio, ohmic contact between FTO and $CuSbS_2$, theoretical simulation details and the formation energies of different point defects in $CuSbS_2$. These materials are available free of charge via the Internet at http://pubs.acs.org.

AUTHOR INFORMATION

Corresponding Authors

*Email: chensy@ee.ecnu.edu.cn.
*Email: jtang@mail.hust.edu.cn.

Notes

The authors declare no competing financial interest.

ACKNOWLEDGMENTS

We would like to acknowledge Prof. Han Huang at the Central South University for UPS measurement assistance. This work was financially supported by the seed project of Wuhan National Laboratory for Optoelectronics (WNLO), the "National 1000 Young Talents" project, the National Natural Science Foundation of China (61274055, 61322401, 61106087, and 91233121), China Postdoctoral Science Foundation (2013M542015), Fundamental Research Funds for the Central Universities, HUST (0118187043, CXY12M008) and special funds for major state basic research (2012CB921401). The authors thank the Analytical and Testing Center of HUST and the facility support of the Center for Nanoscale Characterization and Devices, WNLO.

REFERENCES

(1) Green, M. A.; Emery, K.; Hishikawa, Y.; Warta, W.; Dunlop, E. D. *Prog. Photovoltaics* **2014**, *22*, 1.
(2) Liu, M.; Johnston, M. B.; Snaith, H. J. *Nature* **2013**, *501*, 395.
(3) Mittiga, A.; Salza, E.; Sarto, F.; Tucci, M.; Vasanthi, R. *Appl. Phys. Lett.* **2006**, *88*, 163502.
(4) Wu, Y.; Wadia, C.; Ma, W.; Sadtler, B.; Alivisatos, A. P. *Nano Lett.* **2008**, *8*, 2551.
(5) Puthussery, J.; Seefeld, S.; Berry, N.; Gibbs, M.; Law, M. *J. Am. Chem. Soc.* **2010**, *133*, 716.
(6) Berry, N.; Cheng, M.; Perkins, C. L.; Limpinsel, M.; Hemminger, J. C.; Law, M. *Adv. Energy Mater.* **2012**, *2*, 1124.
(7) Sinsermsuksakul, P.; Hartman, K.; Bok Kim, S.; Heo, J.; Sun, L.; Hejin Park, H.; Chakraborty, R.; Buonassisi, T.; Gordon, R. G. *Appl. Phys. Lett.* **2013**, *102*, 053901.

(8) Scanlon, D. O.; Walsh, A. *Appl. Phys. Lett.* **2012**, *100*, 251911.
(9) Mitzi, D. B.; Gunawan, O.; Todorov, T. K.; Wang, K.; Guha, S. *Sol. Energy Mater. Sol. C* **2011**, *95*, 1421.
(10) Yang, M.; Zakutayev, A.; Vidal, J.; Zhang, X.; Ginley, D. S.; DiSalvo, F. J. *Energy Environ. Sci.* **2013**, *6*, 2994.
(11) Wang, W.; Winkler, M. T.; Gunawan, O.; Gokmen, T.; Todorov, T. K.; Zhu, Y.; Mitzi, D. B. *Adv. Energy Mater.* **2013**, DOI: 10.1002/aenm.201301465.
(12) Shockley, W.; Queisser, H. J. *J. Appl. Phys.* **1961**, *32*, 510.
(13) Zhou, J.; Bian, G.-Q.; Zhu, Q.-Y.; Zhang, Y.; Li, C.-Y.; Dai, J. *J. Solid State Chem.* **2009**, *182*, 259.
(14) Rodriguez-Lazcano, Y.; Nair, M.; Nair, P. *Mod. Phys. Lett. B* **2001**, *15*, 667.
(15) Rodrıguez-Lazcano, Y.; Nair, M.; Nair, P. *J. Cryst. Growth* **2001**, *223*, 399.
(16) Yu, L.; Kokenyesi, R. S.; Keszler, D. A.; Zunger, A. *Adv. Energy Mater.* **2013**, *3*, 43.
(17) Sugaki, A.; Shima, H.; Kitakaze, A. *Technology Reports of Yamaguchi University*; 1973.
(18) Yuan, M.; Mitzi, D. B.; Liu, W.; Kellock, A. J.; Chey, S. J.; Deline, V. R. *Chem. Mater.* **2009**, *22*, 285.
(19) Manolache, S.; Duta, A.; Isac, L.; Nanu, M.; Goossens, A.; Schoonman, J. *Thin Solid Films* **2007**, *515*, 5957.
(20) Rabhi, A.; Kanzari, M.; Rezig, B. *Thin Solid Films* **2009**, *517*, 2477.
(21) Colombara, D.; Peter, L. M.; Rogers, K.; Painter, J.; Roncallo, S. *Thin Solid Films* **2011**, *519*, 7438.
(22) Nair, M.; Pena, Y.; Campos, J.; Garcia, V.; Nair, P. *J. Electrochem. Soc.* **1998**, *145*, 2113.
(23) Colombara, D.; Peter, L. M.; Rogers, K. D.; Hutchings, K. *J. Solid State Chem.* **2012**, *186*, 36.
(24) Rosi, F.; Dismukes, J.; Hockings, E. *Electr. Eng.* **1960**, *79*, 450.
(25) Gudelli, V. K.; Kanchana, V.; Vaitheeswaran, G.; Svane, A.; Christensen, N. E. *J. Appl. Phys.* **2013**, *114*, 223707.
(26) Rodriguez-Lazcano, Y.; Nair, M.; Nair, P. *J. Electrochem. Soc.* **2005**, *152*, G635.
(27) Septina, W.; Ikeda, S.; Iga, Y.; Harada, T.; Matsumura, M. *Thin Solid Films* **2014**, *550*, 700.
(28) Sotaniemi, E.; H, J.; Isoṁ aki, H.; Takkunen, J.; Kaila, J. *Ann. Clin. Res.* **1971**, *3*, 30.
(29) Audrieth, L. F.; Ogg, B. A. *Chem. Hydrazine*; Wiley, 1951.
(30) Ramanathan, K.; Contreras, M. A.; Perkins, C. L.; Asher, S.; Hasoon, F. S.; Keane, J.; Young, D.; Romero, M.; Metzger, W.; Noufi, R.; Ward, J.; Duda, A. *Prog. Photovoltaics* **2003**, *11*, 225.
(31) Chen, S.; Walsh, A.; Gong, X. G.; Wei, S. H. *Adv. Mater.* **2013**, *25*, 1522.
(32) Huang, B.; Chen, S.; Deng, H. X.; Wang, L. W.; Contreras, M. A.; Noufi, R.; Wei, S. H. *IEEE J. Photovoltaics* **2014**, *4*, 477.
(33) Meiying Leng, Y. Z.; Zhe, X.; Jie, Z.; Huaibing, S.; Xinsheng, L.; Bo, Y.; Junpei, Z.; Jie, C.; Kunhao, Z.; Junbo, H.; Yibing, C.; Jiang, T. *Adv. Energy Mater.* **2013**, 201301846.
(34) Mitzi, D. B. *Adv. Mater.* **2009**, *21*, 3141.
(35) Yuan, M.; Mitzi, D. B. *Dalton Trans.* **2009**, 6078.
(36) Liu, W.; Mitzi, D. B.; Yuan, M.; Kellock, A. J.; Chey, S. J.; Gunawan, O. *Chem. Mater.* **2010**, *22*, 1010.
(37) Mitzi, D. B.; Yuan, M.; Liu, W.; Kellock, A. J.; Chey, S. J.; Gignac, L.; Schrott, A. G. *Thin Solid Films* **2009**, *517*, 2158.
(38) Mitzi, D. B.; Kosbar, L. L.; Murray, C. E.; Copel, M.; Afzali, A. *Nature* **2004**, *428*, 299.
(39) Mitzi, D. B.; Copel, M.; Murray, C. E. *Adv. Mater.* **2006**, *18*, 2448.
(40) Liu, W.; Mitzi, D. B.; Yuan, M.; Kellock, A. J.; Chey, S. J.; Gunawan, O. *Chem. Mater.* **2009**, *22*, 1010.
(41) Bob, B.; Lei, B.; Chung, C. H.; Yang, W.; Hsu, W. C.; Duan, H. S.; Hou, W. W. J.; Li, S. H.; Yang, Y. *Adv. Energy Mater.* **2012**, *2*, 504.
(42) Todorov, T. K.; Reuter, K. B.; Mitzi, D. B. *Adv. Mater.* **2010**, *22*, E156.
(43) Todorov, T. K.; Tang, J.; Bag, S.; Gunawan, O.; Gokmen, T.; Zhu, Y.; Mitzi, D. B. *Adv. Energy Mater.* **2013**, *3*, 34.
(44) Milliron, D. J.; Mitzi, D. B.; Copel, M.; Murray, C. E. *Chem. Mater.* **2006**, *18*, 587.
(45) Yang, W.; Duan, H. S.; Bob, B.; Zhou, H.; Lei, B.; Chung, C. H.; Li, S. H.; Hou, W. W.; Yang, Y. *Adv. Mater.* **2012**, *24*, 6323.
(46) Scragg, J. J.; Ericson, T.; Kubart, T.; Edoff, M.; Platzer-Björkman, C. *Chem. Mater.* **2011**, *23*, 4625.
(47) Temple, D. J.; Kehoe, A. B.; Allen, J. P.; Watson, G. W.; Scanlon, D. O. *J. Phys. Chem. C* **2012**, *116*, 7334.
(48) Kyono, A.; Kimata, M. *Am. Mineral.* **2005**, *90*, 162.
(49) Mitzi, D. B.; Yuan, M.; Liu, W.; Kellock, A. J.; Chey, S. J.; Deline, V.; Schrott, A. G. *Adv. Mater.* **2008**, *20*, 3657.
(50) Su, H.; Xie, Y.; Wan, S.; Li, B.; Qian, Y. *Solid State Ionics* **1999**, *123*, 319.
(51) Rossi, A.; Atzei, D.; Da Pelo, S.; Frau, F.; Lattanzi, P.; England, K.; Vaughan, D. *Surf. Interface Anal.* **2001**, *31*, 465.
(52) Partain, L.; Schneider, R.; Donaghey, L.; Mcleod, P. *J. Appl. Phys.* **1985**, *57*, 5056.
(53) Naumkin, A.; Kraut-Vass, A.; Gaarenstroom, S.; Powell, C. *US Secretary of Commerce on behalf of the United States of America*; 2012.
(54) Skinner, B. J.; Luce, F. D.; Makovicky, E. *Economic Geology* **1972**, *67*, 924.
(55) Abaab, M.; Kanzari, M.; Rezig, B.; Brunel, M. *Sol. Energy Mater. Sol. C* **1999**, *59*, 299.
(56) Han, S.-H.; Hermann, A. M.; Hasoon, F.; Al-Thani, H.; Levi, D. *Appl. Phys. Lett.* **2004**, *85*, 576.
(57) Tanaka, K.; Moritake, N.; Uchiki, H. *Sol. Energy Mater. Sol. C* **2007**, *91*, 1199.
(58) Sun, L.; Kazmerski, L.; Clark, A.; Ireland, P.; Morton, D. *J. Vac. Sci. Technol.* **1978**, *15*, 265.
(59) Davis, E.; Mott, N. *Philos. Mag.* **1970**, *22*, 0903.
(60) Rabhi, A.; Kanzari, M.; Rezig, B. *Mater. Lett.* **2008**, *62*, 3576.
(61) Van der Pauw, L. *Philips Tech. Rev.* **1958**, *20*, 220.
(62) Garza, C.; Shaji, S.; Arato, A.; Perez Tijerina, E.; Alan Castillo, G.; Das Roy, T. K.; Krishnan, B. *Sol. Energy Mater. Sol. C* **2011**, *95*, 2001.
(63) Xu, Y.; Schoonen, M. A. *Am. Mineral.* **2000**, *85*, 543.